Structure determination of the $Cu(100)c(2 \times 2)-Mn$ and $Cu(100)c(2 \times 2)-Au$ surface alloy phases by medium-energy ion scattering

1999 J. Phys.: Condens. Matter 11 1889

(http://iopscience.iop.org/0953-8984/11/8/003)

J. Phys.: Condens. Matter **11** (1999) 1889–1901. Printed in the UK PII: S0953-8984(99)99195-6

Structure determination of the Cu(100)c(2 × 2)–Mn and Cu(100)c(2 × 2)–Au surface alloy phases by medium-energy ion scattering

D Brown†, T C Q Noakes‡, D P Woodruff†§, P Bailey‡ and Y Le Goaziou†

† Physics Department, University of Warwick, Coventry CV4 7AL, UK
‡ CLRC Daresbury Laboratory, Daresbury, Warrington WA4 4AD, UK

Received 11 November 1998

Abstract. The substitutional surface alloy phases Cu(100)c(2 × 2)–Mn and Cu(100)c(2 × 2)–Au have been investigated by medium-energy ion scattering (MEIS) using 100 keV H^+ ions. Blocking patterns in the scattered ion yield have been measured for $[\bar{1}\bar{1}\bar{1}]$, $[\bar{1}\bar{2}0]$ and $[\bar{1}\bar{3}0]$ incidence geometries. Simulations of these blocking patterns have been performed for a range of trial structures and the optimum values of the structural parameters obtained are compared with those available from earlier low-energy electron diffraction (LEED) and photoelectron diffraction (PhD) investigations. The MEIS results confirm the presence of rumpling in the outermost alloy layer, with corrugation amplitudes of 0.37 ± 0.06 Å and 0.06 ± 0.04 Å for the CuMn and CuAu surface alloys respectively. This result supports the previously reported anomalously large corrugation for Cu(100)c(2 × 2)–Mn which has been attributed to the local high-spin state of the Mn atoms.

1. Introduction

It is now widely recognized that even on metal surfaces adsorbates can induce reconstruction of the outermost substrate layers, and in the case of metal-on-metal growth intermixing at the interface can lead to distinct alloy phases with no simple analogue in the bulk [1–3]. Surface alloy phases comprising just the one or two outermost surface layers occur even for some combinations of elements that are immiscible in the bulk. Interest in these materials arises from the fact that they may exhibit novel catalytic, electronic or magnetic properties. In the case of the Cu(100) surface, nominal coverages of 0.5 ML of Mn, Pd or Au all lead to a c(2 × 2) surface phase which appears to comprise a single layer of an ordered substitutional alloy [4–8]. Because of the different atomic radii of Cu and these three metallic adsorbates, however, one may anticipate that this alloy phase does not comprise truly coplanar Cu and adsorbate atoms; rather the two species will have slightly different layer spacings relative to the underlying second (pure Cu) layer, and this difference defines a 'corrugation' of the alloy. The magnitude of the corrugation is generally considered to increase with increasing difference in the atomic radii (taken to be half the nearest-neighbour distance in the appropriate elemental metal) of the alloy components [6]. Thus, structural investigations by quantitative low-energy electron diffraction (LEED) indicate that the Pd atoms (radius 1.375 Å) and Cu atoms (1.276 Å) are almost co-planar in the CuPd surface alloy [6], but that the Au atoms (1.442 Å) are displaced outwards by 0.1 Å relative to the Cu atoms in the CuAu surface alloy

§ Author to whom any correspondence should be addressed. Fax: +44 (0)1203 692016; e-mail address: d.p.woodruff@warwick.ac.uk.

0953-8984/99/081889+13$19.50

[7]. However, LEED studies of the Cu(100)c(2 × 2)–Mn surface indicate that this phase exhibits a much larger corrugation, with the Mn atoms displaced outwards relative to the top-layer Cu atoms by 0.3 Å [4], despite the fact that the Mn metallic radius is 1.365 Å, essentially identical to that of Pd. This result has been attributed to an anomalously large effective radius for the Mn atoms in this phase [4] due to the fact that they retain the local high-spin state of the free atom which is quenched in solid metallic Mn [9–12]. For the CuMn and CuAu alloys, further studies by scanned-energy-mode photoelectron diffraction (PhD) have confirmed the structural model given by LEED [5, 8]. Possible overlayer models have been rejected in favour of a substitutional alloy in which the Mn and Au atoms are displaced outwards relative to the top-layer Cu atoms. The structural model, together with definitions of the important structural parameters, are illustrated in figure 1. Despite the general agreement between the LEED and PhD analyses for these alloys, there are small but significant differences in terms of the structural parameters obtained. In particular, there is a clear difference in the values of the interlayer spacing between the Mn or Au atoms and atoms in the second (pure) Cu layer. An independent test of the detailed structural parameters by a complementary technique based on wholly different principles (both LEED and PhD exploit elastic electron scattering) could be beneficial in resolving this discrepancy.

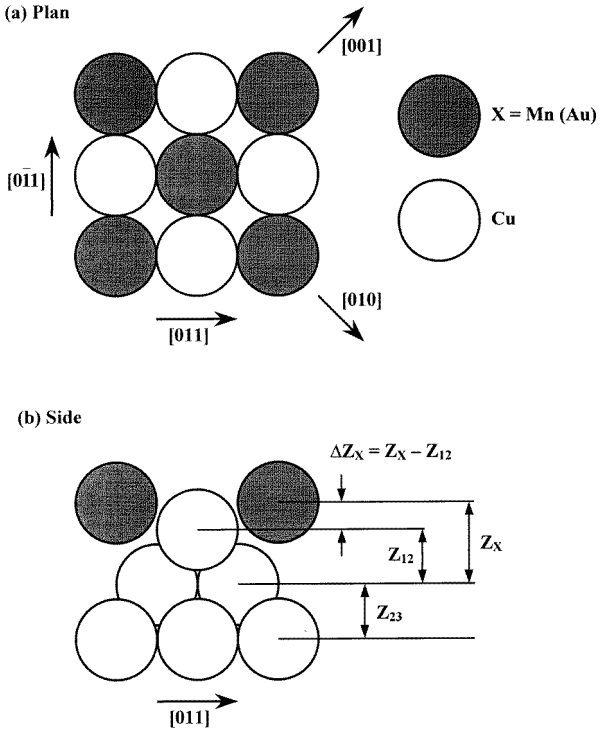

Figure 1. A schematic model showing (a) the plan and (b) side views of the Cu(100)c(2 × 2)–X (X = Mn or Au) surface alloy phases. The structural parameters investigated in the present study are also defined.

Medium-energy ion scattering (MEIS) is a technique that has been employed in the elucidation of a variety of surface structural problems [13], and is most incisive through the use of the so-called double-alignment geometry. In these experiments incident ion beams (typically of H^+ or He^+) in the approximate energy range 50–200 keV are aligned with a specific

crystallographic, or channelling, direction with respect to the sample. This alignment ensures that subsurface atoms are shadowed by near-surface atoms, the actual number of near-surface layers illuminated being dependent on the specific incident geometry chosen. In addition, ions back-scattered from subsurface atoms may be prevented from leaving the sample in certain directions due to blocking by atoms closer to the surface; the resultant dips in the scattered ion yield thus define near-surface interatomic directions. By simulating the scattering experiment for different possible surface structures and optimizing the fit to the experimentally determined angles and shapes of these blocking features, one may therefore determine the surface structure. A more detailed description of the MEIS technique can be found elsewhere [13].

The investigation described in this paper used the recently commissioned (April 1996) UK national MEIS facility to investigate the Cu(100)c(2×2)–Mn and Cu(100)c(2×2)–Au surface alloy phases. Much of the methodology employed is common to previous MEIS studies, but at this new facility we have developed some differences in approach, so we include a significant amount of detail concerning both our experimental methods and our method for establishing the optimum structural model and defining its precision. We then compare the surface structural parameter values obtained in this MEIS investigation with those previously found by LEED and PhD.

2. Experimental details

The experiments described here were performed at the UK national MEIS facility, based at the CCLRC's (Council for the Central Laboratories of the Research Council's) Daresbury Laboratory. The facility comprises a hot-cathode duoplasmatron ion source and accelerator derived from the decommissioned Nuclear Structure Facility, together with an ultrahigh-vacuum (UHV) end-station. The ion source and transfer assembly deliver a beam with a spot size of 0.5×1.0 mm^2 onto the sample. The beam current to the sample is monitored by a measurement of the current arriving at a fine tungsten mesh positioned in the beam path just inside the UHV scattering chamber. The mesh provides 70% transmission and is surrounded by a shield biased at -300 V to suppress secondary-electron loss from the mesh. The end-station consists of separate chambers for storage, sample preparation and scattering measurements, with samples transferable under UHV conditions between the scattering and preparation chambers via the storage chamber. Pumping of these chambers is by rotary-backed turbomolecular pumps and titanium sublimation pumps which routinely achieve base pressures of approximately 1×10^{-10} mbar following a 423 K bake-out. The scattering chamber is fitted with a high-precision goniometer allowing adjustment of sample rotation (about a vertical axis), tilt (about a horizontal axis) and azimuthal angle (about the surface normal) to within 0.1°, together with a toroidal electrostatic energy analyser (TEA). These components, supplied by High-Voltage Engineering, are commercial developments of an original FOM-AMOLF design [14]. Ions scattered from the sample into the TEA are deflected electrostatically through 90° onto a set of channel plates to produce amplified charge pulses which then impinge on a position-sensitive detector plate. The position of arrival in the dispersion plane defines the scattered ion energy, while the position perpendicular to this defines the collection. Processing of the output from this detector thus produces a two-dimensional ion energy–scattering angle map, the angular range being defined by the 24° angular acceptance of the detector. Larger ranges in energy or angle can be obtained by 'tiling' together individual maps obtained for different settings of the analyser potentials or position.

In situ preparation of the Cu(100) sample and the metal overlayers was performed in the sample preparation chamber. Cleaning was effected by cycles of sputtering with 1 keV Ar^+ ions, followed by electron-bombardment annealing to 823 K. The surface composition

and degree of long-range order were determined by Auger electron spectroscopy (using a VG Scientific 100AX spherical sector analyser) and by observation of the LEED pattern respectively. Both Mn and Au were deposited onto clean Cu(100) with the sample maintained at a temperature of approximately 373 K. For the case of Mn deposition, an Oxford Instruments Knudsen cell was employed. A resistively heated W filament wrapped with Au wire was used for deposition of the Au. In each case, following deposition, the initially (1×1) LEED pattern changed to give a sharp c(2×2) pattern with low background.

Ion scattering measurements to obtain blocking curves were performed with the sample at room temperature, employing 100 keV H^+ ions incident along three different directions: $[\bar{1}\bar{1}1]$ (in the $[0\bar{1}\bar{1}]$ azimuth) and along $[\bar{1}\bar{2}0]$ and $[\bar{1}\bar{3}0]$ (in the $[0\bar{1}0]$ azimuth). After obtaining each data set, the sample was moved vertically with respect to the incoming ion beam in order to minimize beam-induced damage. Blocking curves were obtained from the 2D energy–angle maps by integration of the surface peaks and subsequent projection onto the angle axis over an energy range corresponding, approximately, to a depth of five atomic layers. The final data sets used in the subsequent analysis each comprised the sum of two or more individual blocking curves obtained from newly prepared surfaces. At the relatively small scattering angles used in these experiments (26° to 62°) the Cu and Mn surface scattering peaks were unresolved, and even the Cu and Au surface peaks were not fully resolved. The integrations of the surface peaks were therefore conducted such as to include both the Cu and Mn or Au scattering yields. 'Bulk' (subsurface) blocking curves were similarly obtained by integration of the energy–angle maps over a range of scattered ion energies below the surface peaks. The absolute precision of the analyser angular position is only about 1–2°, so the locations of the blocking dips in the bulk blocking curves were used as an internal reference to correct for this source of systematic error in these angles.

3. Results and discussion

MEIS data were obtained for both the Cu(100)c(2×2)–Mn and Cu(100)c(2×2)–Au surface phases as described previously in section 2. Data for the clean Cu(100) surface were also obtained for the purposes of comparison. A typical two-dimensional energy–angle map obtained for incidence along the $[\bar{1}\bar{2}0]$ crystallographic direction from the Cu(100)c(2×2)–Au surface is shown in figure 2. The scale adjacent to the figure shows the sequence of colours used to represent increasing intensity of the scattered ions which is used in the false-colour map. In the upper (high-scattered-energy) part of the map the horizontal (maxima) streaks correspond to the Au and Cu surface peaks. Especially in the lower-intensity lower-energy region below these surface peaks, corresponding to scattering from (and energy loss in) the subsurface, it is also easy to see vertical (minima) streaks corresponding to the $[3\bar{5}0]$, $[1\bar{2}0]$, $[1\bar{3}0]$ and $[1\bar{5}0]$ bulk blocking dips.

Figure 3 shows the integrated surface peak blocking curves obtained from the Cu(100)c(2×2)–Mn surface for ions incident in the $[\bar{1}\bar{1}1]$, $[\bar{1}\bar{2}0]$ and $[\bar{1}\bar{3}0]$ directions. The experimental data have been normalized to account for angular variations in the Rutherford scattering cross-section. In order to extract the details of the surface structure from these data, scattering simulations were conducted using the VEGAS computer code [15]; the effectiveness of this code in simulating MEIS data has been demonstrated in many previous studies by the AMOLF group (e.g. [13]). Calculations were made for a series of trial structures and the best-fit simulation (also shown in figure 3) is assumed to result from a calculation based on the correct structural model. As in all such 'trial-and-error' approaches to surface structure determination (used in almost all techniques with this objective) the identification of the best fit was made through the use of an objective reliability factor or 'R-factor'. In the process of establishing

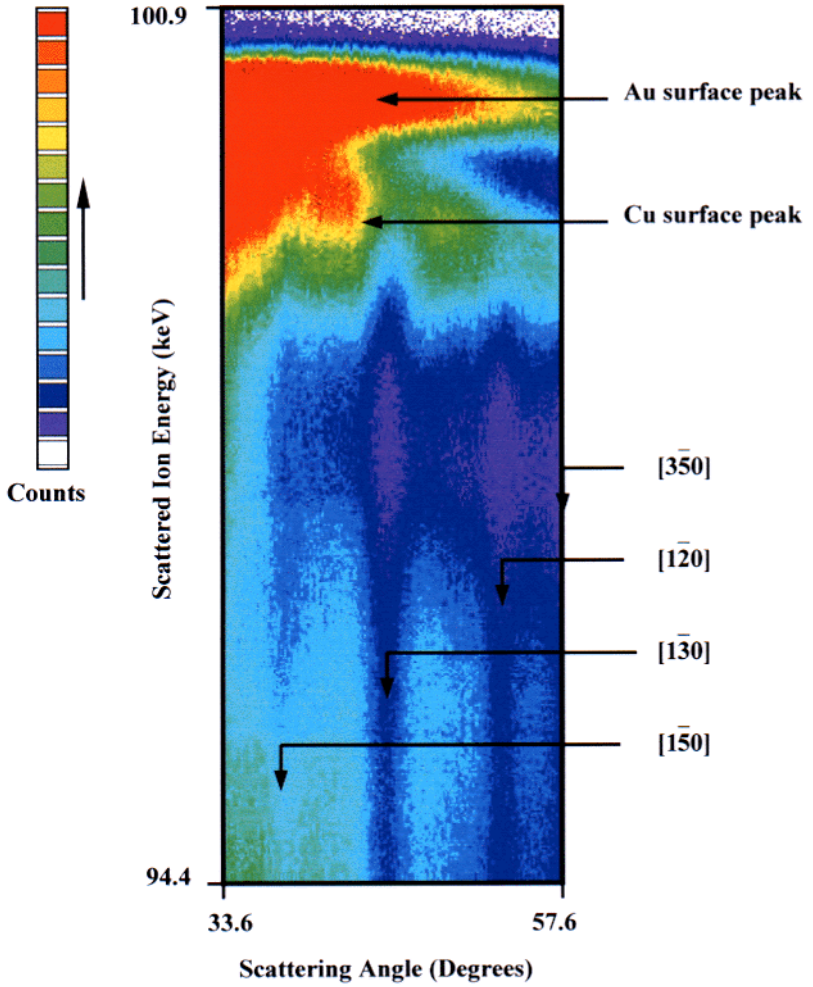

Figure 2. A typical two-dimensional ion energy–scattering angle map obtained from the Cu(100)c(2 × 2)–Au surface obtained with 100 keV H^+ ions incident along the [1̄20] channelling direction. The intensity of back-scattered ions is indicated by the arbitrary false-colour scale. The Cu and Au surface peaks are indicated, together with major blocking features in the scattered ion yield.

our own methodology for MEIS structure determination we have recently presented a general discussion of R-factors for MEIS [16] as well as giving fuller details of the exact approach that we have adopted [17]. Here we summarize the main points and some details specific to the present study.

The specific R-factor that we use is essentially χ-squared:

$$R_\chi = \frac{1}{N}\sum_{i=1}^{i=N}\frac{(Y-\lambda Y_{sim})^2}{Y}. \tag{1}$$

Y and Y_{sim} represent the experimental and simulated yields respectively. Notice that the experimental yield, Y (which appears in the denominator), is an actual number of scattered ions counted, which is therefore an estimate of the square of the standard deviation of the

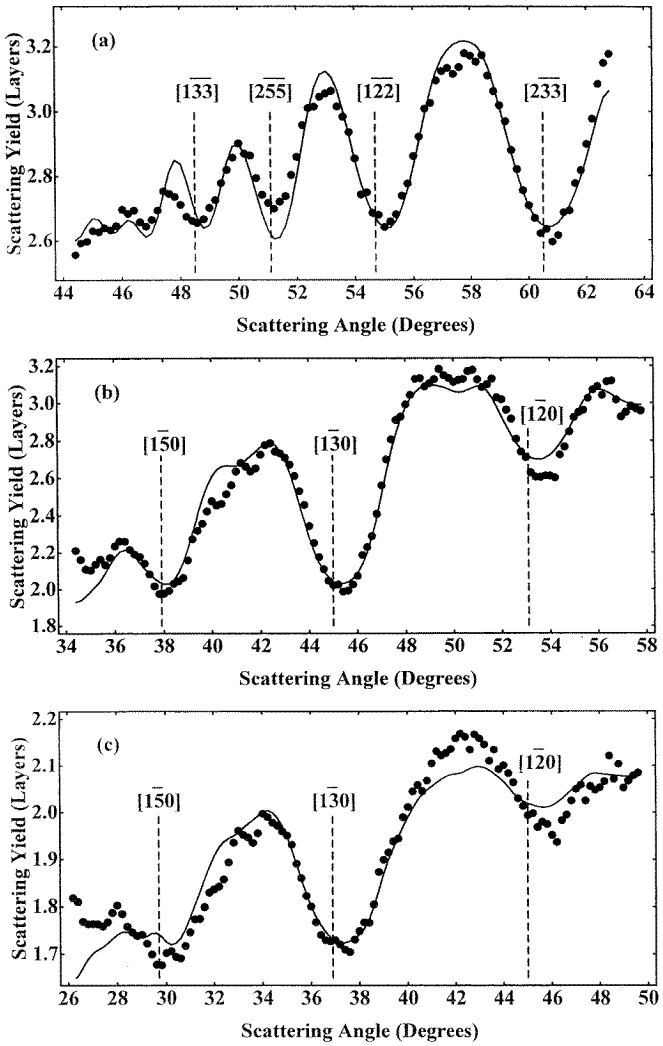

Figure 3. Experimental blocking curves for Cu(100)c(2 × 2)–Mn obtained with 100 keV H^+ ions (data points), together with the corresponding best-fit simulations (solid curves) for (a) [1̄11̄], (b) [1̄20] and (c) [1̄30] incidence directions. The ordinate indicates the number of layers illuminated for each geometry derived in the calculations. Expected positions of blocking minima for a simple, bulk-terminated structure are indicated by dashed curves and annotations in each case.

Poisson noise. For this reason λ, a scaling factor, is applied to the simulated yields which are given in the calculations in terms of the number of atoms (layers) 'seen' by the incident ions per bulk crystallographic 'string' of atoms along the incidence direction. Strictly, λ can be determined in the experiment by proper absolute calibration of the scattering yields, and indeed such absolute calibration is a key ingredient of the MEIS technique. Nevertheless, this calibration is subject to significant systematic errors, so some adjustment of this scaling parameter is normal. In the present case λ was freely adjusted to optimize the fit for each structure tested; we have shown elsewhere [17] that this approach does appear to be justified. Because the VEGAS calculations were run for each of the three incidence directions separately,

the initial experiment–theory comparisons yielded three separate R-factors for each structure. A single global R-factor can be obtained in the form of equation (1) by combining the individual R-factors for each of the experimental geometries, R_{111}, R_{120} and R_{130}, to give

$$R_T = \frac{N_{111}R_{111} + N_{120}R_{120} + N_{130}R_{130}}{N_{111} + N_{120} + N_{130}} \tag{2}$$

where N_{111}, N_{120} and N_{130} represent the numbers of data points in each individual blocking curve.

One general feature that we have found in comparing experimental and theoretical blocking curves for a number of systems is that, even after correcting for the Rutherford scattering cross-sections, there is a systematic trend for the experimental yields to display a slight 'tilt' relative to the simulated ones; while not fully understood this is probably a consequence of some combination of instrumental effects and imprecise cross-sectional scaling. In order to ensure that equal weight is given to all parts of the blocking curves in determining the optimum R-factor the experimental curves were therefore 'levelled' by multiplication by an appropriate third-order polynomial; this correction is typically no more than 5%. Simple smoothing was also applied to the simulated curves to minimize the effect of statistical fluctuations in the Monte Carlo sampling.

As mentioned in the previous section, the Cu and Mn surface scattering peaks were unresolved in the experiment so the integrated blocking curves include scattering from both species. The simulated yields were thus computed to incorporate the combined Cu and Mn signals, corrected for the appropriate difference in scattering cross-section. Calculations were based on a five-layer slab (the nominal integration depth of the experimental data). A Thomas–Fermi–Molière scattering potential was assumed. Note that in the VEGAS code this potential is used to calculate the shadow cones and the weak scattering associated with trajectories near the shadow-cone edge for which the screening of the Coulomb potential is important, but the scattering cross-section of the main 'hard' collision is not included in the output. It is for this reason that the experimental data must be corrected to account for the angular dependence of the scattering cross-section in this hard collision; for this purpose the unscreened Rutherford cross-section appears to be adequate. The structural search involved variation of the Mn-atom height above the second Cu layer (Z_{Mn}), together with top-to-second-layer (Z_{12}) and second-to-third-layer (Z_{23}) Cu spacings (figure 1). Initially, both Z_{Mn} and Z_{12} were varied between 1.4 and 2.2 Å in 0.1 Å increments and Z_{23} varied between 1.6 and 2.0 Å, also in 0.1 Å increments.

As expected, MEIS was found to be sensitive to the magnitude of the interlayer spacings and the magnitude, but not the sign, of the corrugation. By combining the Cu and Mn scattering yields we effectively lose the ability to distinguish between Cu atoms above Mn and Mn atoms above Cu in the surface alloy for two atoms with such similar ion scattering cross-sections. In fact LEED is also likely to be very insensitive to this difference because this technique can only distinguish the two elements by their different electron elastic scattering cross-sections which are very similar, and the published LEED study did not appear to include in its structural search the site inversion of Cu and Mn in the top layer of the optimum structures [4]. Nevertheless, the PhD investigation [5], which did have elemental specificity and so can readily distinguish these two situations, confirmed the conclusions of the LEED study that the Mn atoms do lie above the plane of the top-layer Cu atoms. We therefore did not regard this aspect of the structure as contentious, and assumed that the corrugation was positive (Mn displaced outwards).

Having established the optimum parameter values on the 0.1 Å grid, further simulations were then performed to fine-tune the structural optimization, utilizing progressively smaller ranges and incremental differences (down to 0.01 or 0.02 Å) in the structural parameters. All of the simulations assumed uncorrelated, isotropic thermal vibrations and no attempt was made to conduct a detailed optimization of their amplitudes. Typically, vibrational amplitudes

Table 1. A summary of the structural parameter values obtained in this MEIS study for Cu(100)c(2 × 2)–Mn. For definitions of the structural parameters refer to figure 1. The results of previous LEED [4] and PhD [5] studies are also shown for comparison.

Parameter (Å)	LEED [4]	PhD [5]	MEIS
Z_{Mn}	2.09 ± 0.02	2.02 ± 0.04	2.09 ± 0.04
Z_{12}	1.79 ± 0.02	1.63 ± 0.08	1.72 ± 0.04
Z_{23}	1.80 ± 0.03	1.83 ± 0.08	1.83 ± 0.02
ΔZ_{Mn}	0.30 ± 0.02	0.39 ± 0.08	0.37 ± 0.06

in the outermost surface layer are 50–100 % higher than the corresponding bulk values, the enhancement decaying rapidly over one or two layers [18, 19]. In order to establish the sensitivity of our results to the treatment of the thermal vibrations, two sets of simulations were performed. In the first set, the root mean square vibrational amplitudes of the top-layer atoms were assumed to be 50% greater than the corresponding bulk value of 0.09 Å for Cu [20]. In the second set, a 100% vibrational enhancement of the top-layer atoms was assumed. The optimized structural parameters obtained from these two sets of simulations differed by no more than 0.01 or 0.02 Å, well within the limits of the associated uncertainties. The best-fit structural parameter values obtained in this way are given in table 1.

As discussed previously [17], the precision in the structural parameters obtained in this

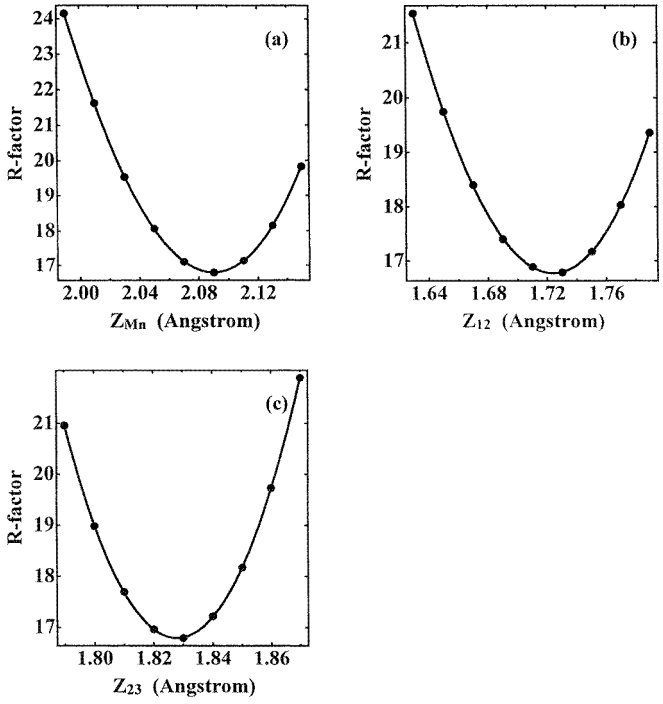

Figure 4. Plots of the overall R-factor, R_T, for each of the structural parameters (a) Z_{Mn}, (b) Z_{12} and (c) Z_{23} for the Cu(100)c(2 × 2)–Mn surface. The smooth curves, used to evaluate the curvature at the minima and thus to estimate the precision, are the results of fitting a fifth-order polynomial to the data points in each case.

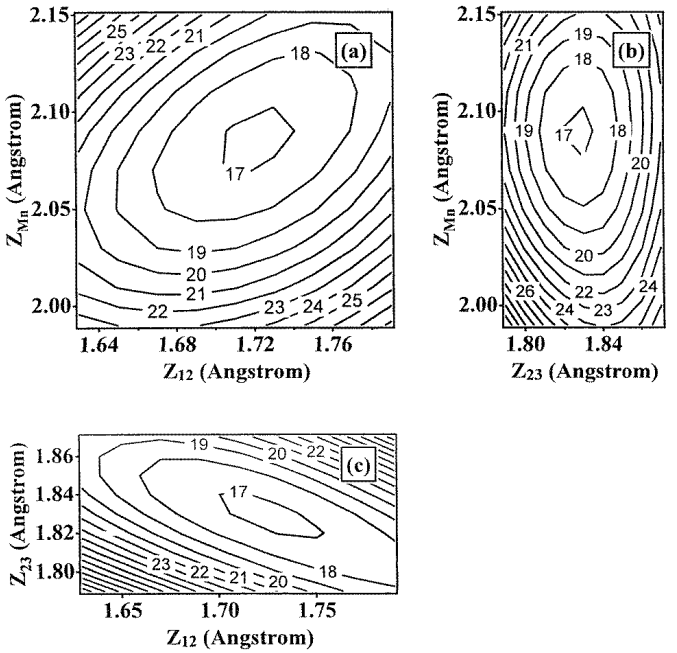

Figure 5. *R*-factor variations illustrated as contour plots for each combination of the structural parameters investigated for Cu(100)c(2 × 2)–Mn: (a) Z_{Mn}/Z_{12}, (b) Z_{Mn}/Z_{23} and (c) Z_{23}/Z_{12}. The corresponding *R*-factor values are indicated adjacent to the contour lines.

way ($\pm\sigma$) can be determined from the variation of the *R*-factor value around its minimum value, R_{min}, as a function of the appropriate structural parameter, Z, according to the relationship [21]

$$\frac{2}{\sigma^2} = \left(\frac{d^2 R_\chi}{dZ^2}\right)_{R=R_{min}}. \tag{3}$$

Variations in the overall *R*-factor for each of the structural parameters optimized in the simulations are shown as the data points in figures 4(a)–4(c). Solid curves represent a smooth fit to the data obtained with a fifth-order polynomial which were used to evaluate the second-order differentials of equation (3), allowing the precision estimates shown in table 1 to be made. We should note, however, that the precision of single parameters is only truly meaningful if the parameters are not coupled; i.e. if the *R*-factor increase produced by shifting one parameter from its optimum value cannot be then reduced by changing a second parameter value. If this kind of parameter coupling occurs, the true precision may be worse than implied by this standard analysis, or the precision may be better expressed in other ways. Information relating to this problem is provided by the *R*-factor contour plots for each pair of the structural parameters Z_{Mn}, Z_{12} and Z_{23} shown in figures 5(a)–5(c) for Cu(100)c(2 × 2)–Mn. Parameter coupling in such plots is characterized by contours of constant *R*-factor values which are ellipses skewed along diagonals. Figure 5(b) is characterized by contours which show no skew away from the principal axes, so the optimum value of Z_{Mn} (corresponding to the minimum in the *R*-factor) is essentially independent of the value of the parameter Z_{23}. Z_{Mn} can thus be optimized independently of Z_{23}. Figures 5(a) and 5(c), on the other hand, do show some parameter coupling; a particular consequence of this is that the true global minimum in the *R*-factor (and thus the best-fit parameter values) can only be achieved by simultaneous optimization of these parameters.

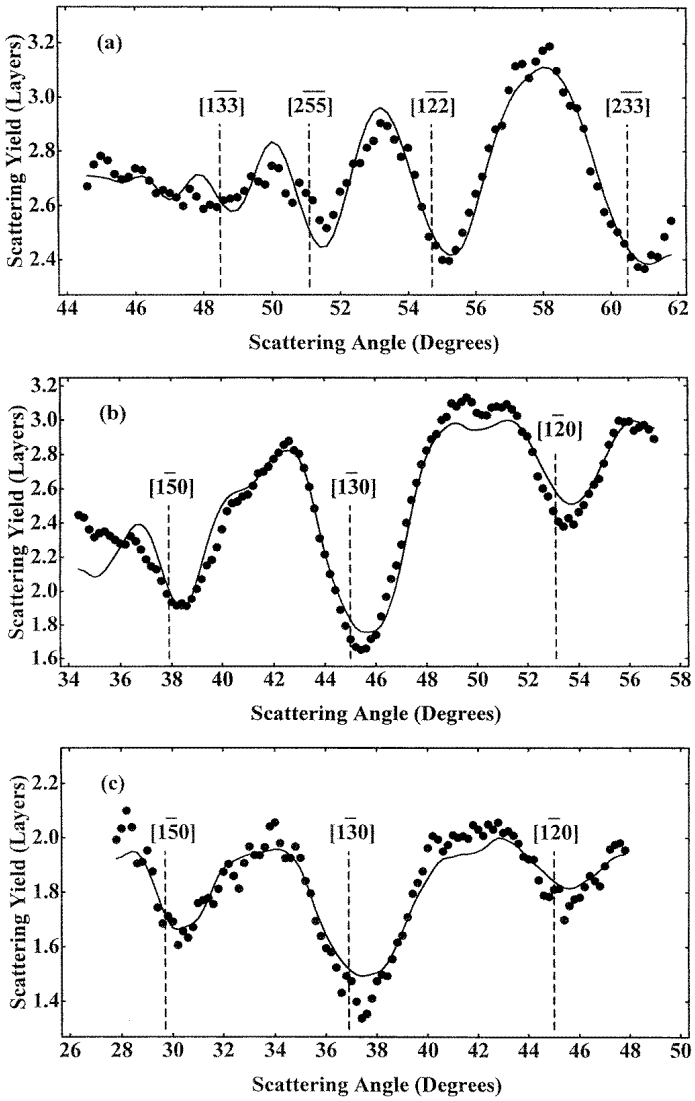

Figure 6. Experimental blocking curves obtained from the Cu(100)c(2 × 2)–Au surface using 100 keV H^+ incident ions, together with the corresponding best-fit simulations for incidence along (a) $[\bar{1}\bar{1}\bar{1}]$, (b) $[\bar{1}\bar{2}0]$ and (c) $[\bar{1}\bar{3}0]$. Details are as described in the caption to figure 3.

Figure 6 shows a similar comparison of experimental blocking curves with the best-fit simulations for the Cu(100)c(2 × 2)–Au surface, again recorded in the $[\bar{1}\bar{1}\bar{1}]$, $[\bar{1}\bar{2}0]$ and $[\bar{1}\bar{3}0]$ incidence geometries. The structural optimization followed essentially the same procedure as that described for the Cu(100)c(2 × 2)–Mn surface. Figures 7 and 8 show corresponding *R*-factor curves and contour plots respectively for the Cu(100)c(2 × 2)–Au structural parameters. Notice that while, unlike the case for the scattering from the Cu and Mn surface atoms, there was some spectral separation of the surface scattering peaks from Cu and Au (see figure 2), these two poorly resolved features were also combined in the integration of the surface peak, but in this case the large mass difference does lead to a significant sensitivity to the sign of the

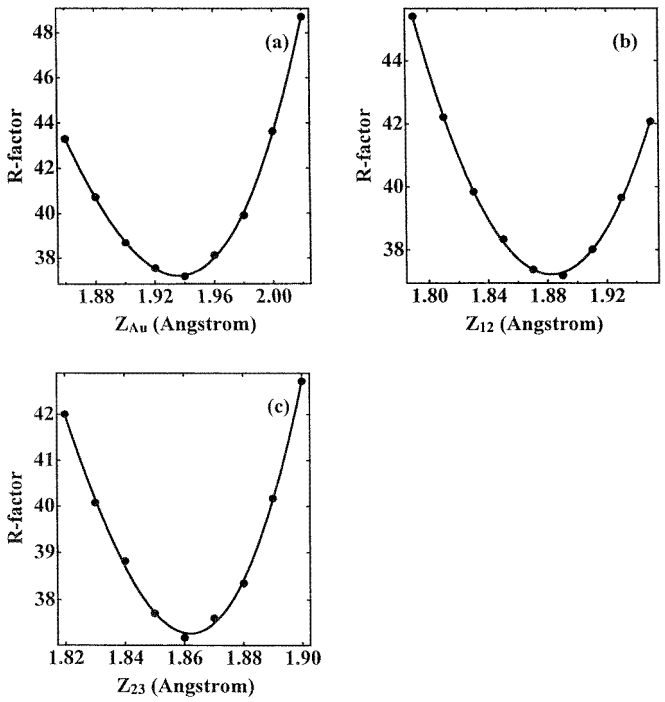

Figure 7. Overall R-factor curves for Cu(100)c(2 × 2)–Au obtained from comparison of experimental data and simulations for each of the structural parameters (a) Z_{Au}, (b) Z_{12} and (c) Z_{23}. In each case the smooth curves have been obtained by fitting a fifth-order polynomial to the data points.

surface corrugation (as seen in figure 8(a)).

Tables 1 and 2 show the best-fit structural parameter values, together with the associated uncertainties, determined in this study, for Cu(100)c(2 × 2)–Mn and Cu(100)c(2 × 2)–Au respectively. Corresponding structural parameters derived from earlier LEED and PhD studies are also listed for comparison. In making these comparisons it is worth noting that the three techniques have intrinsically different sensitivities to different parameters. In particular, LEED is especially sensitive to the surface layer spacings relative to the underlying substrate, and MEIS is sensitive to the relative layer spacings of the uppermost layers. LEED is not intrinsically element specific, while although MEIS has this potential, the lack of substrate and

Table 2. A summary of the structural parameter values obtained in the present MEIS investigation of the Cu(100)c(2 × 2)–Au surface, together with results previously obtained by LEED [7] and PhD [8]. Definitions of the structural parameters are provided in figure 1. The asterisk indicates an *assumed* value.

Parameter (Å)	LEED [7]	PhD [8]	MEIS
Z_{Au}	1.98	1.88	1.94 ± 0.03
Z_{12}	1.88	1.78	1.88 ± 0.03
Z_{23}	1.807*	1.71	1.86 ± 0.02
ΔZ_{Au}	0.10	0.10	0.06 ± 0.04

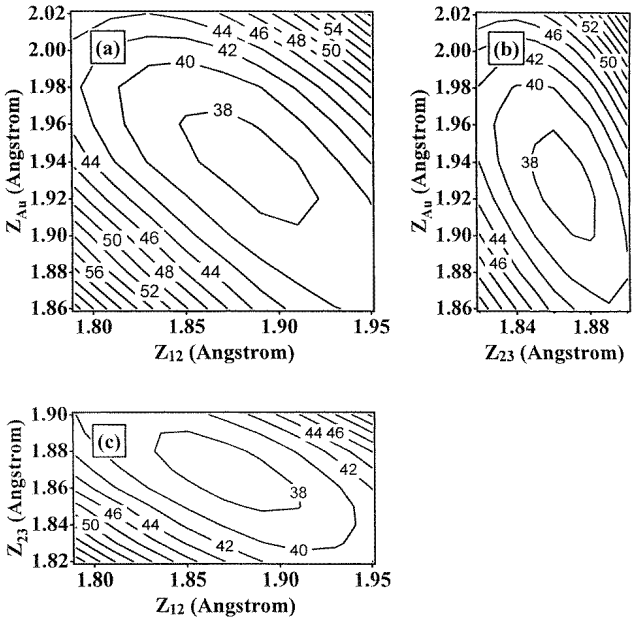

Figure 8. *R*-factor variations for Cu(100)c(2 × 2)–Au illustrated as contour plots for each pair of structural parameters (a) Z_{Au}/Z_{12}, (b) Z_{Au}/Z_{23} and (c) Z_{23}/Z_{12}. *R*-factor values are indicated adjacent to the contour lines.

adsorbate scattering peak separation means that this potential was not exploited here. Notice, however, that if the adsorbate occupies only the outermost layer, even this potential is not useful because the adsorbate scattering displays no blocking. Finally we note that the PhD studies, concentrating on emission from the adsorbate Mn or Au atoms, are sensitive mainly to the layer spacing of this adsorbate species relative to the underlying substrate layers. None of the techniques used are *directly* dependent on the surface layer corrugation.

We first consider the results for the Cu(100)c(2 × 2)–Mn surface alloy phase. The MEIS results fail to fully resolve the differences between the LEED and PhD studies. For example, although the MEIS value for Z_{Mn} is the same as that found by LEED, while these differ by 0.07 ± 0.06 Å from the PhD value, the MEIS value for Z_{12} lies midway between those obtained by LEED and PhD although, taking account of the quoted precisions, the MEIS value is actually in formal disagreement with that found by LEED. All three methods agree in the value of Z_{23} to within their estimated precision, these values being within about 1% of the bulk value. Finally, we note that all three methods yield a similar large (approximately 0.35 Å) corrugation of the outermost layer; while the optimum value found in MEIS is closer to that obtained from PhD, all three values are within one standard deviation of each other.

In the case of the Cu(100)c(2 × 2)–Au surface phase, comparisons are more difficult due to the lack of cited precision in the earlier LEED and PhD studies although the PhD investigation was based only on a single normal-emission spectrum and so must also suffer from a significant problem of uniqueness in the solution. Overall, in this case, the MEIS gives consistently better agreement with LEED than with this restricted PhD study and, in particular, fails to reproduce the large (0.10 Å) contraction of the second-to-third-layer spacing. On the other hand, the three values of the surface alloy layer corrugation are in good agreement for a value much smaller (approximately 0.10 Å) than that found for Cu(100)c(2 × 2)–Mn.

4. Conclusions

Interest in the two-dimensional surface alloy phases Cu(100)c(2×2)–Mn and Cu(100)c(2×2)–Au stems in part from the fact that these *are* surface alloys, but also particularly from the fact that the surface corrugations in the two systems indicate that the Mn atoms behave as though they are larger than Cu or Au, an effect attributed to the fact that the Mn atoms in this system retain their local high-spin state of the free atom [4]. This structural result, previously obtained in independent LEED and PhD investigations, is confirmed by our MEIS study, which yields very similar values for the two corrugation amplitudes of 0.37 ± 0.06 Å and 0.06 ± 0.04 Å respectively. In the case of the Cu(100)c(2 × 2)–Mn surface some quantitative discrepancies between the previous LEED and PhD studies are not fully resolved, the values deduced by MEIS agreeing best with different techniques for different parameters. In the case of the Cu(100)c(2 × 2)–Au surface the parameter values found by MEIS are much closer to those found by LEED than in the previous PhD study based on a very small data set. In this case, however, the lack of clear estimates in the earlier experiments means that it is not possible to attach a formal significance to this disagreement.

Acknowledgments

The authors are pleased to acknowledge the financial support of EPSRC for the DL MEIS facility and the Warwick-based research programme. The VEGAS simulation code was supplied by courtesy of the FOM Institute for Atomic and Molecular Physics, Amsterdam. Vital technical support was also provided at DL by Mr Brian Blackwell and Dr Kevin Connell.

References

[1] Woodruff D P 1994 *J. Phys.: Condens. Matter* **6** 6067
[2] King D A and Woodruff D P (ed) 1994 *Phase Transitions and Adsorbate Restructuring of Surfaces (The Chemical Physics of Solid Surfaces vol 7)* (Amsterdam: Elsevier)
[3] King D A and Woodruff D P (ed) 1997 *The Growth and Properties of Ultrathin Epitaxial Layers (The Chemical Physics of Solid Surfaces vol 8)* (Amsterdam: Elsevier).
[4] Wuttig M, Gauthier Y and Blugel S 1993 *Phys. Rev. Lett.* **70** 3619
[5] Toomes R, Theobald A, Lindsay R, Geibel T, Schaff O, Didszhun R, Woodruff D P, Bradshaw A M and Fritzsche V 1996 *J. Phys.: Condens. Matter* **8** 10 231
[6] Wu S C, Lu S H, Wang Z Q, Lok C K C, Quinn J, Li Y S, Tian D, Jona F and Marcus P M 1988 *Phys. Rev.* B **38** 5363
[7] Wang Z Q, Li Y S, Lok C K C, Quinn J and Jona F 1987 *Solid State Commun.* **62** 181
[8] Tobin J G, Hansen J C and Wagner M K 1990 *J. Vac. Sci. Technol.* A **8** 2494
[9] O'Brien W L, Zhang J and Tonner B P 1993 *J. Phys.: Condens. Matter* **5** L515
[10] O'Brien W L and Tonner B P 1994 *J. Appl. Phys.* **76** 6468
[11] O'Brien W L and Tonner B P 1995 *Phys. Rev.* B **51** 617
[12] Hayden A B, Pervan P and Woodruff D P 1995 *J. Phys.: Condens. Matter* **7** 1159
[13] van der Veen J F 1985 *Surf. Sci. Rep.* **5** 199
[14] Tromp R M, Copel M, Reuter M C, Horn von Hoegen M, Speidell J and Koudijs R 1991 *Rev. Sci. Instrum.* **62** 2679
[15] Tromp R M and Van der Veen J F 1983 *Surf. Sci.* **133** 159
[16] Noakes T C Q, Bailey P and Woodruff D P 1998 *Nucl. Instrum. Methods* B **136–138** 1125
[17] Bailey P, Noakes T C Q and Woodruff D P 1999 submitted
[18] Chester M and Gustafsson T 1991 *Surf. Sci.* **256** 135
[19] Fowler D E and Barth J V 1995 *Phys. Rev.* B **52** 2117
[20] Gemmel D S 1974 *Rev. Mod. Phys.* **46** 129
[21] Bevington P R 1969 *Data Reduction and Error Analysis for the Physical Sciences* (New York: McGraw-Hill)